BIOCHEMISTRY
including biophysical chemistry & molecular biology

Article

pubs.acs.org/biochemistry

The Conserved Trp−Cys Hydrogen Bond Dampens the "Push Effect" of the Heme Cysteinate Proximal Ligand during the First Catalytic Cycle of Nitric Oxide Synthase

Jérôme Lang,[†] Jérôme Santolini,[‡] and Manon Couture*,[†]

[†]Département de biochimie, de microbiologie et de bioinformatique, PROTEO and IBIS, pavillon Charles-Eugène Marchand, room 3163, Université Laval, Québec, Canada G1V 0A6

[‡]Laboratoire de Stress Oxydant et Détoxication, iBiTec-S, Commissariat à l'Energie Atomique, Saclay, Gif-sur-Yvette 91191 Cedex, France

S *Supporting Information*

ABSTRACT: Residues surrounding and interacting with the heme proximal ligand are important for efficient catalysis by heme proteins. The nitric oxide synthases (NOSs) are thiolate-coordinated enzymes that catalyze the hydroxylation of L-Arg in the first of the two catalytic cycles needed to synthesize nitric oxide. In NOSs, the indole NH group of a conserved tryptophan [W56 of the bacterial NOS-like protein from *Staphylococcus aureus* (saNOS)] forms a hydrogen bond with the heme proximal cysteinate ligand. The purpose of this study was to determine the impact of increasing (W56F and W56Y variants) or decreasing (W56H variant) the electron density of the proximal cysteinate ligand on molecular oxygen (O_2) activation using saNOS as a model. We show that the removal of the indole NH···S$^-$ bond for W56F and W56Y caused an increase in the electron density of the cysteinate. This was probed by the decrease of the midpoint reduction potential ($E_{1/2}$) along with weakened σ-bonding and strengthened π-backbonding with distal ligands (CO and O_2). On the other hand, the W56H variant showed stronger Fe−OO and Fe−CO bonds (strengthened σ-bonding) along with an elevated $E_{1/2}$, which is consistent with the formation of a strong NH···S$^-$ hydrogen bond from H56. We also show here that changing the electron density of the proximal thiolate controls its "push effect"; whereas the rates of both O_2 activation and autoxidation of the $Fe^{II}O_2$ complex increase with the stronger push effect created by removing the indole NH···S$^-$ hydrogen bond (W56F and W56Y variants), the W56H variant showed an increased stability of the complex against autoxidation and a slower rate of O_2 activation. These results are discussed with regard to the roles played by the conserved tryptophan−cysteinate interaction in the first catalytic cycle of NOS.

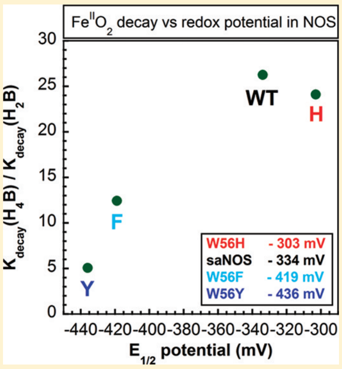

Nitric oxide synthases (NOSs) are thiolate-coordinated heme proteins that catalyze the two-step oxidation of the amino acid L-arginine (L-Arg) to L-citrulline and nitric oxide ($^\bullet$NO) with molecular O_2 and NADPH as cosubstrates. They are present in both the eukaryotic and prokaryotic kingdom. The best-characterized NOSs are the three isoforms found in mammals. $^\bullet$NO synthesized by the endothelial NOS (eNOS), neuronal NOS (nNOS), and inducible NOS (iNOS) isoforms act in various physiological processes such as the regulation of blood pressure, signal transmission in the nervous system, and the production of nitrosative stress by the immune system.[1−4] All mammalian NOS isoforms are homodimers that share two common structural regions known as the oxygenase domain (NOS_{ox}) and the C-terminal reductase domain (NOS_{red}). NOS_{ox} contains the binding site for the catalytic heme center, which is coordinated to the sulfur atom of a cysteinate residue. On the opposite side of the thiolate coordination, the active site comprises the binding site for the substrate L-Arg in the proximity of the heme Fe where O_2 binds. The cofactor (6*R*)-tetrahydrobiopterin (H_4B) that is required for $^\bullet$NO synthesis forms a radical as it provides an electron for O_2 activation during catalysis. NOS_{red} has binding sites for NADPH and two flavin cofactors (FAD and FMN). The latter transfers electrons from NADPH to NOS_{ox}. Connecting the two domains and regulating the flow of electrons from NOS_{red} to NOS_{ox} is a calmodulin (CaM)-binding region.[4−7]

NOSs are present not only in mammals and other higher organisms but also in a subset of bacteria such as *Staphylococcus aureus* (saNOS), *Bacillus subtilis* (bsNOS), *Bacillus anthracis* (baNOS), and *Deinococcus radiodurans* (drNOS) and the thermophilic species *Geobacillus stearothermophilus* (gsNOS).[8−10] These enzymes are structurally related to the oxygenase domain of mammalian NOSs with an overall highly conserved three-dimensional structure.[11−15] However, striking differences distinguish the mammalian and bacterial NOSs. First, the bacterial NOSs are smaller than their mammalian counterparts as they lack the C-terminal reductase domain. The electrons from NADPH necessary for catalysis may transit to the bacterial NOS via various redox partners that may not

Received: June 23, 2011
Revised: October 20, 2011
Published: October 24, 2011

dx.doi.org/10.1021/bi200965e | *Biochemistry* 2011, 50, 10069−10081

normally be associated with •NO production[16] except for the NOS of *Sporangium cellulosum*. This NOS has an N-terminal domain, which contains a [2Fe-2S] ferredoxin-like subdomain and binding sites for FAD and NADPH, that is fused to the NOS domain and allows the production of •NO from NADPH and NADH in the presence of H_4B or tetrahydrofolate.[17] Second, the zinc-binding site of the mammalian NOSs found at the dimer interface is absent in the bacterial enzymes. With regard to the nature of the redox active cofactor, as most bacteria containing a *nos* gene lack the sepiapterin reductase gene necessary for H_4B synthesis, another cofactor such as tetrahydrofolate may be used by the bacterial NOSs.[8,18−20] Both of these cofactors support the synthesis of •NO or a •NO-related compound in vitro. The in vivo production of •NO, or a •NO-related compound, has been demonstrated for some bacteria.[21−23] The range of biological activities of the bacterial NOSs appears to be varied.[9] NO produced by the NOS of *D. radiodurans* acts as a transcriptional regulator for growth recovery after exposure to UV radiation.[23] In *B. subtilis* and *B. anthracis*, the NOS appears to protect bacilli against oxidative stress through the suppression of the Fenton reaction and the direct activation of catalase. In addition, the *NOS* gene of *B. anthracis* is essential for spore virulence.[22,24] Interestingly, Gusarov et al. demonstrated that bacterial *nos* gene provides an increased level of protection against a wide spectrum of antibiotics.[25] Despite these differences, much evidence points to a common catalytic mechanism of the bacterial and mammalian NOS. The substrates L-Arg and N^{ω}-hydroxy-L-Arg (NOHA) are recognized with high affinity by both types of enzymes. These substrates bind in the same location at the active site and form similar hydrogen bonding interactions with conserved residues.[13,14,26]

The conversion of L-Arg to citrulline and •NO is a two-step mechanism that requires three electrons to complete the chemistry.[1,3] The first step necessitates two electrons and converts L-Arg to NOHA, while the second converts NOHA to citrulline and •NO using one electron globally, although a second electron is transiently needed during the course of the reaction. For both of these steps, the initial event is the reduction of the heme Fe^{III} to heme Fe^{II} followed by the binding of an oxygen molecule (O_2) to generate the oxygenated complex ($Fe^{II}O_2$). From there, the hydroxylation of L-Arg to the NOHA intermediate requires a second electron provided by the pterin cofactor and is believed to be performed by a compound I species, i.e., a ferryl heme with an associated radical ($Fe^{IV}{=}O\ \pi^{+\bullet}$). For the second catalytic step, the pterin cofactor transiently provides an electron to aid in the formation of the active species involved in the conversion of NOHA to L-citrulline and •NO, which may be the hydroperoxy complex (Fe^{III}−OOH).[27−31] Alternative scenarios have been proposed for both steps of the catalytic cycle (reviewed in refs 31 and 32).

It is relatively well established that the proximal ligand (cysteinate) is crucial for O_2 activation and catalysis in heme−thiolate protein.[33,34] Residues surrounding and interacting with the cysteine S^- and the heme play an important role in the stability of the active site as well as during catalysis. In NOSs, a conserved tryptophan residue in the proximal binding loop forms π−π stacking interactions with the heme and supplies a hydrogen bond from its indole NH group to the sulfur atom of the deprotonated proximal cysteine (Figure S1 of the Supporting Information). Several groups, including us, have studied the structure−function relationship of this Trp in bacterial[35,36] and mammalian NOSs (mNOSs).[36−42] We recently characterized the $Fe^{II}CO$ and $Fe^{III}NO$ complexes of W56F and W56Y variants of the NOS of *S. aureus* (saNOS) by optical and resonance Raman spectroscopy and demonstrated that the Trp56−Cys interaction has a structural and electronic role in regulating the thiolate ligand basicity similar to that in mNOS.[36] A similar study that was also recently conducted with Trp66 variants of the NOS-like protein of *B. subtilis* also points out a structural and electronic role for the Trp−Cys interaction.[35] In theory, the OH group of Y56 of saNOS could provide a hydrogen bond to the cysteine sulfur. However, with W56Y of saNOS as with W60Y of bsNOS, there is no evidence that this occurs in $Fe^{II}CO$ and $Fe^{III}NO$ complexes.[35,36]

Over the past several years, our characterization of the saNOS enzyme by resonance Raman spectroscopy revealed how the substrates L-Arg and NOHA interact with heme-bound ligands (CO and •NO[43,44]), including the physiological ligand O_2.[45,46] The purpose of this study was to look at the impact of increasing or decreasing the electron density of the proximal cysteinate ligand on the catalytic properties of NOS during the first catalytic cycle and to correlate these with the spectroscopic features of the oxygenated complex ($\nu_{\text{Fe−OO}}$ and $\nu_{\text{O−O}}$ modes). In this regard, mutations at position 56 (W56F, W56Y, and W56H) were designed to minimize changes in the π−π stacking interactions with the heme. We used the W56F and W56Y variants of the bacterial saNOS that display increased electron density of the axial cysteine as a consequence of the removal of the hydrogen bond involving the indole nitrogen of W56 and the sulfur of C62.[36] In light of the report by Stuehr's group that a W188H variant of $iNOS_{ox}$ was able to form a hydrogen bond with the axial cysteine that is stronger than that originating from W188 of the WT enzyme,[47] we generated the analogous W56H variant of saNOS (the W66H variant of bsNOS was independently obtained by one of us[35]). If indeed H56 is able to form a strong hydrogen bond in saNOS, as it does in bsNOS[35] and iNOS,[47] this variant would complement our previous work with the W56F and W56Y variants and may allow generation within the same protein framework a set of variants that may display increased (W56F and W56Y[36]) and decreased (W56H) electron density of the axial cysteine, which would allow the investigation of the impact of the thiolate electron density on O_2 activation. These variants provide evidence that changing the basicity of the cysteinate ligand modifies the "push effect" with a direct impact on the kinetics of activation of the oxygenated complex by H_4B and the kinetics of autoxidation of the oxygenated complex.

■ EXPERIMENTAL PROCEDURES

Chemicals. L-Arg was obtained from Alexis Biochemicals (QBiogene, Carlsbad, CA). H_4B and H_2B were obtained from Schircks laboratories (Jona, Switzerland). Sodium dithionite was purchased from Fluka (Sigma-Aldrich, Oakville, ON). Argon, $^{12}C^{16}O$ gas, and $^{16}O_2$ gas were purchased from Praxair (Mississauga, ON). $^{13}C^{18}O$ and the $^{18}O_2$ isotope were purchased from Icon Isotopes (Summit, NJ). Redox indicators (phenosafranin and benzyl and methyl viologen) were purchased from Sigma-Aldrich (Lyon, France).

Mutagenesis. Site-directed mutagenesis of the saNOS coding sequence was performed as described previously.[36,48] The W56H mutation was confirmed by sequencing at a local facility.

Protein Expression, Purification, and Storage. WT saNOS and the W56 variants were expressed in *Escherichia coli* cells and purified as described previously.[36,43] The heme *b* was quantified via the pyridine hemochrome method as described by Appleby.[49] All sample concentrations are reported on the basis of heme concentrations. The proteins were dialyzed against a 40 mM HEPES buffer (pH 7.6) containing 150 mM NaCl, 1 mM DTT, and 10% glycerol and stored at −80 °C.

Affinity for L-Arg. The affinity of saNOS and the W56H variant for L-Arg was obtained from the titration of the ferric proteins with L-Arg at equilibrium. Binding of L-Arg induced large optical absorption changes that reflect the transition from a six-coordinate low-spin heme to the five-coordinate high-spin state. These were used to calculate the concentration of the L-Arg-bound complex of these NOSs, [RL]. The [RL] versus [L] data were then fitted to eq 1[50] using Kaleidagraph (Synergy Software, Reading, PA):

$$[\mathrm{RL}] = \Big[[\mathrm{RL}] + [\mathrm{L}] + K_\mathrm{d} - \sqrt{([\mathrm{R}] + [\mathrm{L}] + K_\mathrm{d})^2 - 4[\mathrm{R}][\mathrm{L}]}\Big]/2 \qquad (1)$$

where R is the protein, RL is the NOS−L-Arg complex, L is the ligand (L-Arg), and K_d is the equilibrium dissociation constant.

The heme of the W56F and W56Y variants in the ferric state is mostly five-coordinate and high-spin in the absence of added substrate. To determine an apparent K_d [$K_{\mathrm{d(app)}}$], a six-coordinate complex was first formed by the addition of 1 mM imidazole. Titration with L-Arg then afforded a transition to the five-coordinate high-spin state as L-Arg displaced the bound imidazole. The changes in absorbance induced by L-Arg binding (shift of the Soret band from 427 to 398 nm) were used to calculate the concentration of the L-Arg-bound NOSs, [RL]. The plot of [RL] as a function of the concentration of L-Arg was fitted to eq 1 to determine an apparent K_d. We did not attempt to calculate the true K_d from these data as the competitive binding of L-Arg and imidazole may not behave as expected for a two-state model.[51] The protein concentration was 5 μM.

Preparation of the Sample for Spectroscopy. All experiments were conducted at room temperature (20−25 °C) in 40 mM HEPES buffer (pH 7.6) containing 40 mM NaCl. For samples containing L-Arg and pterins, the following concentrations were used: 1 mM L-Arg, 1 mM H_2B, and 1 mM H_4B.

Absorption Spectroscopy. $\mathrm{Fe^{II}CO}$ complexes of the saNOS W56H variant were prepared as described previously.[36] Briefly, the protein solutions were made anaerobic by being flushed with argon. A known volume of gaseous CO was then injected into the cuvette, and the heme was reduced by addition of a small volume of a freshly prepared anaerobic solution of sodium dithionite. Optical absorption spectra were recorded with a Cary 3 spectrophotometer with samples placed in a 1 cm path-length anaerobic cuvette (Hellma, Müllheim, Germany). The samples were prepared at a concentration of 5 μM based on heme.

Resonance Raman Spectroscopy. The resonance Raman acquisitions of the $\mathrm{Fe^{II}CO}$ complexes of W56H were recorded as previously reported using the 442 nm line of a He/Cd laser (Liconix laser, Melles-Griot, Ottawa, ON) with an excitation power of ≈3 mW.[36] These spectra were used to investigate changes in the strength of the proximal ligand that occur upon mutations at position 56. We did not measure directly the strength of the Fe−S bond in the ferric state. This determination requires the acquisition of resonance Raman spectra with near-UV laser excitation, which is a technology unavailable in our laboratory. The spectra were analyzed with Grams (ThermoGalactic, Salem, NH). Regression analysis of the Raman lines was performed with a mixed Lorentzian/Gaussian function without any restrictions in terms of peak position, width at half-height, or Lorentzian/Gaussian ratio. Optical spectra were recorded before and after the acquisition of resonance Raman spectra to verify the stability of the $\mathrm{Fe^{II}CO}$ complexes. The experiments were performed at room temperature (20−25 °C) with a sample concentration of 50 μM. The resonance Raman spectra were calibrated with the lines of indene.

Stopped-Flow Spectroscopy. Single-turnover kinetics were studied by stopped-flow spectroscopy conducted inside an anaerobic glovebox (MBraun LabMaster 100) with an Applied Photophysics (Leatherhead, U.K.) SX.18MV stopped-flow spectrometer. A 10 mm path-length cell was used for data acquisition, and the estimated dead time of the stopped-flow apparatus was approximately 1.5 ms. Briefly, anaerobic samples (5 μM) were reduced with 2 equiv of sodium dithionite (10 μM), and an optical spectrum was recorded to confirm that the reduction of the heme was complete. The reduced samples were mixed with O_2 concentrations increasing from 5 to 100%. We used the value of 1356 μM for the dissolved O_2 concentration of O_2-saturated water at 1 atm for the calculation of the bimolecular rate constants for O_2 binding.[52] The experiments were performed at 20 °C.

The kinetics of formation and decay of the oxygenated complex were followed either at single wavelengths or in the kinetic scanning mode where single-wavelength kinetic traces were recorded at 5 nm intervals from 460 to 380 nm and used to generate an optical spectrum-versus-time data set. The latter data set was analyzed using the Specfit global analysis software (Spectrum Software Associates, Chapel Hill, NC) with a three-species kinetic model ($A \rightarrow B \rightarrow C$) with species A corresponding to the initial reduced form, B to the transient oxygenated complex, and C to the final ferric form (noncatalytic condition, with or without Arg and with or without H_2B) or with a four-species model ($A \rightarrow B \rightarrow C \rightarrow D$) when two rates of decay were apparent under catalytic conditions (with Arg and H_4B). A model with concurrent rates for the decay to the ferric state from a single optical species ($\mathrm{Fe^{II}O_2}$ complex, species B) cannot be handled properly by Specfit. To test the concurrent versus sequential models for the decay of the $\mathrm{Fe^{II}O_2}$ complex to the ferric state, we obtained the rates of decay from the fits of single-wavelength kinetics at 440 nm to (1) a model with two concurrent exponentials and (2) a model with two sequential exponentials. The rates determined from both models were the same (the rates with the concurrent model are reported in Table 2) and were also the same as those obtained from global analysis with the sequential ($A \rightarrow B \rightarrow C \rightarrow D$) model (Table 2). The rates determined from global analysis and the fits of single-wavelength kinetic traces were used to calculate the reported mean rates and standard deviations. With L-Arg and H_4B, the faster rate of decay corresponds to the rate of O_2 activation [$k_{\mathrm{decay}}(\mathrm{H_4B})$] while the slower rate, similar in value to the rate of decay of the oxygenated complex determined from the L-Arg/H_2B samples, likely corresponds to the fraction of the oxygenated complex that underwent autoxidation to the ferric state [$k_{\mathrm{decay}}(\mathrm{H_2B})$].

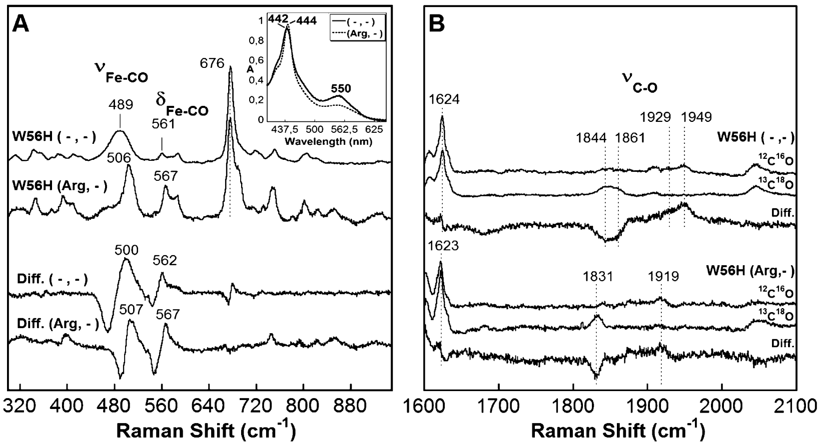

Figure 1. Resonance Raman spectra of the $Fe^{II}CO$ complex of W56H in the absence and presence of L-Arg. (A) Low-frequency region of the resonance Raman spectra with $^{12}C^{16}O$ of substrate-free W56H (−, −) and of L-Arg-bound W56 (Arg, −). Diff. (−, −) and Diff. (Arg, −) are the $^{12}C^{16}O$ spectra minus the $^{13}C^{18}O$ difference spectra of substrate-free and L-Arg-bound W56H, respectively. The inset shows the optical spectra of the $Fe^{II}CO$ complex of W56H in the absence (—) and presence (···) of L-Arg. (B) Very high frequency region of the resonance Raman spectra with the $^{12}C^{16}O$ and $^{13}C^{18}O$ isotopes. The difference spectra (Diff.) correspond to the $^{12}C^{16}O$ minus $^{13}C^{18}O$ spectra of substrate-free W56H (−, −) and L-Arg-bound W56H (Arg, −).

Table 1. Resonance Raman Frequencies of the Fe−C−O and C−O Modes of saNOS and the W56 Variants[a]

protein	condition	ν_{Fe-CO} ($^{13}C^{18}O$) (cm^{-1})	δ_{Fe-CO} ($^{13}C^{18}O$) (cm^{-1})	ν_{C-O} ($^{13}C^{18}O$) (cm^{-1})	Soret (nm)	ref
WT saNOS	(−, −)	482 (470)	560 (543)	1930 (1843)	444	43
		497 (481)		1949 (1857)		
	(Arg, −)	502.5 (490)	567 (548)	1917 (1830)	446	this work and ref 43
	(Arg, H_4B)	502 (490)	565 (547)	ND[b]	446	36 and 43
W56H	(−, −)	482 (469)	561 (543)	1929 (1844)	442	this work
		497 (482)		1949 (1861)[c]		
	(Arg, −)	506 (494)	567 (548)	1919 (1831)	444	this work
	(Arg, H_4B)	505 (ND[b])	566 (ND[b])	ND[b]	444	this work
W56F	(Arg, H_4B)	500 (ND[b])	565 (ND[b])	undetectable	449	36
W56Y	(Arg, H_4B)	500 (ND[b])	565 (ND[b])	undetectable	449	36

[a] A regression analysis of all Fe−C−O modes was performed with mixed Lorentzian/Gaussian function without any restrictions in terms of frequency, width at half-height, or Lorentzian/Gaussian ratio using Grams. Values in this table are those obtained from the regression analysis. [b] Not determined. [c] The superimposed $^{13}C^{18}O$ spectra of WT saNOS and W56H spectra are nearly identical. The apparent 4 cm^{-1} upshift for W56H (1861 cm^{-1}) with respect to saNOS (1857 cm^{-1}) appears to arise solely from the regression analysis and may not be significant.

Resonance Raman with a Continuous-Flow Mixer. Construction of the homemade continuous-flow mixer was previously described by Chartier et al.[45] The current version has a dead time of approximately 1−2 ms. Briefly, the reduced form of the W56 variants was obtained by equilibrating the samples (80 μM) with pure argon gas for 30 min at room temperature (20−25 °C) followed by the addition of 2 equiv of sodium dithionite (160 μM). An optical spectrum of the sample (visible region) was acquired prior to the experiment to confirm the complete reduction of the heme. A buffer saturated with 100% O_2 ($^{16}O_2$ or $^{18}O_2$) before mixing was used for the experiments with W56F and W56Y, while concentrations of 10 and 50% were used for W56H in the absence and presence of L-Arg, respectively. Prior to the experiments, the continuous-flow mixer was incubated with a solution of 10 mM sodium dithionite to make it anaerobic. It was then washed with anaerobic buffer to eliminate the excess dithionite. The 442 nm line of a He/Cd laser (Liconix laser, Melles-Griot, Ottawa, ON) was used to probe the oxygenated complex with an excitation power of ~9.0 mW focused on the sample in the detection cell. Typically, several 60 s spectra were recorded at room temperature and averaged with Grams (ThermoGalactic). The resonance Raman spectrum of reduced myoglobin was recorded at the beginning of each experiment to compare and correct the resonance Raman spectra for small differences that arise between calibrations on different days.

Spectroelectrochemistry. UV−visible-mediated spectroelectrochemical titrations of WT saNOS and the W56 variants were performed in a homemade two-compartment bulk electrolysis cell as described previously.[53,54] The working electrode was a gold grid; the auxiliary electrode was a Pt wire, and the reference electrode was a DRIREF-2 Ag/AgCl/KCl 3M model (World Precision Instruments; $E° = 0.210$ V vs NHE; $T = 20$ °C). All potentials are given versus NHE. The cell was maintained under a positive argon pressure during the entire experiment and kept at a constant temperature, 20 °C. Samples for the redox titration experiments were prepared in 100 mM NaCl/40 mM Hepes buffer (pH 7.6) with saturating concentrations of L-Arg (1 mM). The final protein concentration was 30 μM. Samples were washed by two successive cycles of dilution and centrifugation in this final buffer using a Millipore membrane filter (30 kDa cutoff) at 4 °C. The titration was performed with combinations of various mediators, including methyl viologen (10 μM; $E°' = -0.657$ V vs NHE), benzyl viologen (20 μM; $E°' = -0.567$ V vs NHE), and phenosafranin (20 μM; $E°' = -0.428$ V vs NHE).

Electrolysis was conducted under stirring and using a homemade potentiostat as described previously.[54] Oxidative titration from −550 to 0 mV was then performed before the potential was swept negatively to re-reduce the protein. Depending on the conditions, the potentiometric titration was monitored at 406 nm (phenosafranin isosbestic point) or 450 nm (benzyl viologen and methyl viologen isosbestic point). The data were analyzed using the following Nernst equation:

$$\text{fraction}(\text{Fe}^{\text{II}}) = \{\exp[(E^{\circ\prime} - E_{\text{m}}) \times nF/RT] + 1\}^{-1}$$

where n is the number of electrons, E_{m} is the applied potential, and $E^{\circ\prime}$ is the midpoint potential of interest ($F = 96500$ C/mol; $R = 8.31$ J mol^{-1} K^{-1}). Fitted values of n ranged from 0.75 to 1.34 for WT saNOS and the W56 variants, indicating that the redox process involved one electron. R^2 values were ≥ 0.996.

RESULTS

Optical Absorption Spectra of W56H. The optical absorption spectra of W56H displayed a Soret band maximum centered at 442 nm (444 nm with L-Arg) (Figure 1A, inset), which is typical of thiolate-coordinated Fe$^{\text{II}}$CO complexes (P450 state), with only a negligible fraction of a Soret band centered near 420 nm. An absorption band near 420 nm would be an indication that an inactive form, often termed the P420 state, was formed as the proximal cysteine became protonated or was replaced with a histidine.[55] The P420 state may arise for substrate-free and pterin-free NOS samples, but this is not the case here with W56H. Interestingly, the Soret band of W56H is blue-shifted by 2 nm from that of WT saNOS in the absence (444 nm) or presence of L-Arg (446 nm) (not shown), which is the opposite of the 2 nm red shift observed for W56F and W56Y[36] (Table 1). We suggested that the 2 nm red shift of W56F and W56Y was caused by an increased electronic density of the axial thiolate.[56,57] Accordingly, the 2 nm blue shift detected with W56H saNOS is consistent with a decreased electron density of the thiolate as a result of the formation of a strong NH···S$^-$ bond (vide infra). Analogous variants of bsNOS[35] and eNOS[36] exhibit the same behavior. It thus appears that the optical Soret transition is a sensitive marker of the electron density of the proximal cysteinate of NOS.

Affinity for the Substrate L-Arg. The equilibrium dissociation constant (K_{d}) of WT saNOS and the W56H variant was obtained from the titration of the ferric proteins with increasing concentrations of L-Arg. When L-Arg bound, the coordination and spin state of the heme shifted from the six-coordinate and low-spin state (Soret band near 415 nm) to the five-coordinate and high-spin state (Soret band at 397 nm) (Figure S2 of the Supporting Information). W56H displayed a 5-fold lower affinity for L-Arg ($K_{\text{d}} = 4.5$ μM) than WT saNOS (Table S3 and Figure S2 of the Supporting Information). The heme of the ferric W56F and W56Y variants is predominantly in the five-coordinate and high-spin state (not shown). This precluded the direct determination of the affinity for L-Arg. The affinity was estimated from the apparent K_{d} [$K_{\text{d(app)}}$] for the displacement of heme-imidazole species by L-Arg. W56F and W56Y displayed 1.5−5.5-fold higher apparent affinities for L-Arg than WT saNOS (Table S3 and Figure S3 of the Supporting Information). These results show that the W56 variants display variations in their affinities for L-Arg but all have low-micromolar affinities for L-Arg.

Resonance Raman Spectra of the Fe$^{\text{II}}$CO Complex of W56H. Heme proteins have a high affinity for gaseous molecules such as CO, $^{\bullet}$NO, and O_2 because each of these can effectively accept a heme Fe$^{\text{II}}$ dπ electron into their π^* orbitals (π-backbonding).[58] The Fe$^{\text{II}}$CO complex is well-characterized and widely used to probe the active site because CO forms stable complexes with heme and is sensitive to polar and steric interactions with surrounding residues.[58,59] These interactions weaken or strengthen π-backbonding of heme Fe with CO, which is revealed by the frequency of the C−O stretching mode.[60] Backbonding may also be modulated by variations in the basicity of the proximal trans ligand to the heme.[60] The basicity of the proximal trans ligand not only affects π-backbonding but also modulates σ-bonding with exogenous ligands (O_2, $^{\bullet}$NO, and CO).[60] We are using this series of variants to determine if mutations at position 56 modulate the basicity of the proximal cysteinate ligand and in turn could affect σ-bonding and π-backbonding with the distal CO ligand.

We have determined the frequencies of the $\nu_{\text{Fe−CO}}$, $\nu_{\text{C−O}}$, and $\delta_{\text{Fe−C−O}}$ modes of the Fe$^{\text{II}}$CO complexes of the W56H variant. Results for W56F and W56Y were reported previously.[36] The Fe−CO and C−O stretching frequencies ($\nu_{\text{Fe−CO}}$ and $\nu_{\text{C−O}}$, respectively) of W56H were determined with ^{12}C^{16}O and ^{13}C^{18}O (Figure 1 and Table 1). The low-frequency region of the Raman spectrum (Figure 1A) of substrate-free W56H displays isotope sensitive lines best observed in the ^{12}C^{16}O minus ^{13}C^{18}O difference spectrum (diff −, −). The line centered at 489 cm^{-1} with ^{12}C^{16}O (500 cm^{-1} in the difference spectrum) is in the region corresponding to the $\nu_{\text{Fe−CO}}$ mode. Regression analysis revealed that it contains two lines assigned to two $\nu_{\text{Fe−CO}}$ modes at 482 and 497 cm^{-1} based on the amplitude of their isotopic shifts with ^{13}C^{18}O (Table 1). These frequencies are nearly identical to those of WT saNOS (Table 1). The third isotope sensitive line centered at 561 cm^{-1} (562 cm^{-1} in the difference spectrum) was assigned to the Fe−C−O bending mode ($\delta_{\text{Fe−C−O}}$) (Figure 1A). In the very high frequency region (Figure 1B), an isotope sensitive line near 1949 cm^{-1} was shifted to ~1850 cm^{-1} with ^{13}C^{18}O. Regression analysis revealed two lines positioned at 1929 and 1949 cm^{-1} that shifted to 1844 and 1861 cm^{-1}, respectively, with ^{13}C^{18}O (Figure 1B). These lines, at the same frequencies as the two $\nu_{\text{C−O}}$ modes of WT saNOS and relatively similar in proportion, were assigned to the $\nu_{\text{C−O}}$ modes of W56H (Table 1). Overall, these results show a very similar heme environment of the Fe$^{\text{II}}$CO complexes of substrate-free W56H and WT saNOS.

We repeated these studies in the presence of substrate (L-Arg) to determine the frequencies of the Fe−C−O modes of substrate-bound W56H. Two isotope sensitive lines were detected in the low-frequency region [Figure 1A (Arg, −)]. The line centered at 506 cm^{-1} (507 cm^{-1} in the difference spectrum) was attributed to $\nu_{\text{Fe−CO}}$, while the line at 567 cm^{-1} (567 cm^{-1} in the difference spectrum) was assigned to $\delta_{\text{Fe−C−O}}$ (Figure 1A). With respect to WT saNOS, the $\nu_{\text{Fe−CO}}$ frequency of W56H is 3 cm^{-1} higher but that of $\delta_{\text{Fe−C−O}}$ is identical (Table 1). In the very high frequency region [Figure 1B (Arg, −)], W56H displayed an isotope sensitive line centered at 1919 cm^{-1} (1831 cm^{-1} with ^{13}C^{18}O) that was assigned to the C−O stretching mode. This frequency is 1−2 cm^{-1} higher than that of WT saNOS (Table 1). As observed previously with WT saNOS, the effect of H_4B was modest.[43] Its binding decreased slightly (~1 cm^{-1}) the frequencies of both the Fe−CO stretching mode and the Fe−C−O bending mode of W56H (Table 1). These results reveal that $\nu_{\text{Fe−CO}}$ of L-Arg-bound W56H was upshifted by 3 cm^{-1} and $\nu_{\text{C−O}}$ was also upshifted by 1−2 cm^{-1}. Overall, the $\nu_{\text{Fe−CO}}$ frequency of the L-Arg-bound W56 variants decreases in the following order: W56H > WT > W56Y ∼ W56F[36] (Table 1).

Redox Potentiometry Measurements. Modulation of the electronic density on the thiolate bond in the W56 mutants likely affects the heme midpoint reduction potential.[47] The potentiometric titration assays of WT saNOS and the W56 variants were conducted in the presence of L-Arg; under this condition, the heme adopts a five-coordinate and high-spin state (ref 43 and results not shown). The inset of Figure 2 shows the optical absorption spectra recorded at the various potentials applied to drive the oxidized−reduced transition of WT saNOS (straight lines) and of the mediator (benzyl viologen, dotted lines). As one can see, the spectral region near 450 nm features large spectroscopic changes arising from the oxidized−reduced transition of the heme; in comparison, the changes arising from the mediator redox state remain negligible. The absorbance changes of the other mediators (phenosafranin and methyl viologen) were also negligible under the conditions we used for the W56 variants. The spectral transitions of WT saNOS and its W56 variants, obtained at 450 or 406 nm, were plotted against their corresponding applied potential (millivolts) and fitted to a one-electron Nernst function (Figure 2). The calculated heme midpoint reduction potential ($E_{1/2}$) of WT saNOS (− 334 ± 1 mV) decreased by 80−100 mV to −419 ± 1 mV (W56F) and −436 ± 1 mV (W56Y) for the W56 variants with no hydrogen bond from residue 56. On the other hand, $E_{1/2}$ increased by 31 mV to −303 mV for the W56H variant. These results show that in this system, the heme midpoint redox potentials decrease in the same order (W56H > WT > W56F > W56Y) as the $\nu_{\text{Fe−CO}}$ frequencies (W56H > WT > W56Y ∼ W56F).

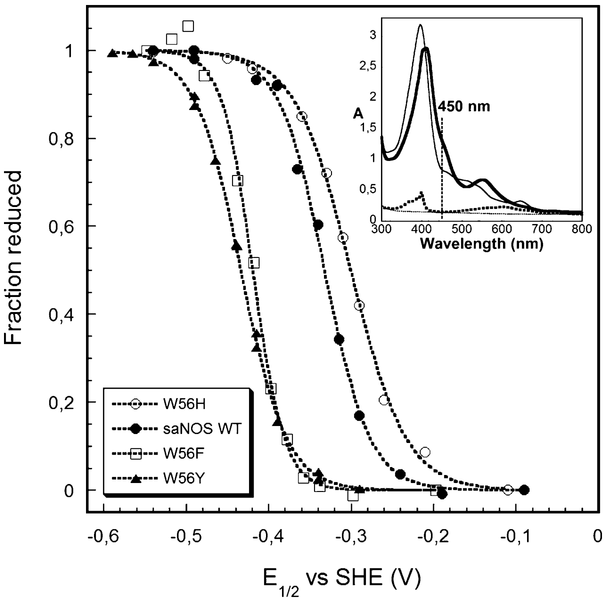

Figure 2. Heme midpoint redox potential ($E_{1/2}$) of L-Arg-bound WT saNOS and the W56 variants. The changes in the protein redox equilibrium (fraction oxidized), plotted as a function of the applied potential (millivolts), were fitted through a one-electron Nernst function. The fitted $E_{1/2}$ values are −303 ± 1 mV for W56H, −334 ± 1 mV for saNOS, −419 ± 1 mV for W56F, and −436 ± 1 mV for W56Y. The inset shows the spectral transition near 450 nm for WT saNOS as the ferric state (thin solid line) is reduced to the ferrous state (thick solid line) and as the redox active mediator benzyl viologen (thin dotted line) is reduced (thick dotted line). The redox indicator phenosafranin was used in potentiometric titrations of W56H, and methyl viologen was used for W56F and W56Y.

Kinetics of Formation and Decay of the Fe^{II}O$_2$ Complex. Stopped-flow experiments were conducted to examine the relation between the kinetics of formation and decay of the oxygenated complex (Fe^{II}O$_2$) and the electron density of the proximal cysteinate. The kinetics of formation and decay of the Fe^{II}O$_2$ complex were acquired from single-turnover kinetics performed under catalytic conditions (with L-Arg and H_4B) and noncatalytic conditions (with L-Arg and H_2B or with L-Arg alone) (Table 2). In NOSs, the oxygenated complex is formed after O_2 binds to the reduced heme. Its activation is then initiated by the transfer of one electron from the cofactor H_4B.[47] H_2B is the oxidized form of the pterin cofactor H_4B that lacks the ability to transfer electrons to activate the oxygenated complex.[14,47,61] In the presence of H_2B, the oxygenated complex autoxidizes to the ferric state when superoxide dissociates from the heme. The use of H_2B and H_4B thus allows the determination of the rate of autoxidation of Fe^{II}O$_2$ (with H_2B) and the rate of O_2 activation (with H_4B) of pterin-bound and L-Arg-bound NOS. Under noncatalytic conditions, a three-species kinetic model (A → B → C) was used to fit the data, with species A corresponding to the initial chemically reduced protein (Fe^{II}), species B to the transient oxygenated complex (Fe^{II}O$_2$), and species C to the final ferric form of the protein (Fe^{III}). Under catalytic conditions, a four-species model was used (A → B → C → D) because the oxygenated intermediate decayed with two apparent rates to the ferric state.

Figure 3 is a representative figure showing the stopped-flow results obtained from mixing chemically reduced W56H with O_2 under catalytic conditions (L-Arg- and H_4B-bound W56H). Figure 3A shows a set of original optical spectra recorded over a time course of 10 s. The kinetic traces (raw data) and the fits to the kinetic traces obtained from the four-state sequential model (A → B → C → D) by global analysis are shown at the wavelengths that correspond to the disappearance of the reduced state (415 nm), the buildup of the Fe^{II}O$_2$ complex (440 nm), and, finally, the decay of the Fe^{II}O$_2$ complex and the concomitant buildup of the ferric five-coordinate state [395 nm (Figure 3B)]. The transition from the Fe^{II}O$_2$ complex (species B) to the ferric state (species C and D of the four-state model) is best modeled with two rates (Table 2). The data fitted nicely to the kinetic model as the amplitudes of the residuals were less than 0.001 absorbance unit at all wavelengths (not shown). Rates of decay similar to those from the global analysis were obtained when the Fe^{II}O$_2$ to ferric state transition was modeled with single-wavelength kinetic data with two concomitant exponentials (Table 2) or two sequential exponentials (not shown). The optical spectra obtained from global analysis (Figure 3C) match the actual spectra of the reduced species (solid line), the Fe^{II}O$_2$ species (dotted line), and the ferric species (dashed lines). These stopped-flow experiments were repeated for WT saNOS and the three W56 variants. The calculated optical spectra from the global analysis revealed that the optical spectrum of the Fe^{II}O$_2$ complex (species B) was similar for all three variants (Figure S4 of the Supporting Information) and displayed a Soret band ranging from 427 to 430 nm under all conditions tested like WT saNOS. The W56

Table 2. Rates of Formation and Decay of the Oxygenated Complex of saNOS and Its W56 Variants in the Presence of Substrate L-Arg

protein	k_{on}[a] ($\times 10^6$ M^{-1} s^{-1})	rate of formation,[b,d] k_{obs} (s^{-1})	rate of decay[c,d] (global analysis), k_{obs} (s^{-1})	rate of decay[c,e] (single wavelength), k_{obs} (s^{-1})
saNOS (Arg, −)	1.2 ± 0.1	518 ± 43	ND[f]	1.6 ± 0.1 (20.4 ± 5.5)[g]
saNOS (Arg, H_2B)	ND[f]	587 ± 54	0.97 ± 0.03	0.86 ± 0.03
saNOS (Arg, H_4B)	1.3 ± 0.2	452 ± 43	ND[f]	22.6 ± 4.9
				2.6 ± 0.1
W56F (Arg, −)	1.2 ± 0.3	438 ± 45	12.6 ± 0.4	9.7 ± 1.2
W56F (Arg, H_2B)	ND[f]	414 ± 38	5.7 ± 0.2	5.6 ± 0.1
W56F (Arg, H_4B)	1.0 ± 0.2	366 ± 45	82.9 ± 8.3	69.7 ± 7.4
			10.0 ± 0.9	7.8 ± 0.4
W56Y (Arg, −)	1.0 ± 0.2	340 ± 43	33.1 ± 1.5	27.9 ± 2.0
W56Y (Arg, H_2B)	ND[f]	397 ± 13	17.4 ± 0.3	17.2 ± 0.3
W56Y (Arg, H_4B)	0.8 ± 0.2	351 ± 43	87.6 ± 22.4	87.7 ± 24.7
			13.9 ± 1.4	16.7 ± 1.5
W56H (Arg, −)	0.9 ± 0.2	315 ± 14	0.34 ± 0.01	0.33 ± 0.01
W56H (Arg, H_2B)	ND[f]	330 ± 38	0.20 ± 0.01	0.17 ± 0.01
W56H (Arg, H_4B)	0.7 ± 0.1	255 ± 25	4.2 ± 0.4	4.1 ± 0.4
			0.61 ± 0.03	0.61 ± 0.06

[a] The k_{on} values were obtained by linear regression of the rates of formation of the oxygenated complex obtained from global analysis plotted at different O_2 concentrations. The following O_2 concentrations were used: 25, 50, 75, and 100% (before mixing). [b] The experiments were performed in 50% O_2-saturated buffer before mixing (678 μM). The rates of formation obtained from global analysis represent the mean of at least three independent experiments each comprised of at least three kinetic data sets. The values reported are the means ± the standard deviation. [c] The rates of decay represent the means of a minimum of three independent experiments each comprised of at least three kinetic data sets. The values reported are the means ± the standard deviation. They correspond to autoxidation under noncatalytic conditions [(Arg, −) or (Arg, H_2B)] and O_2 activation under catalytic conditions (Arg, H_4B). [d] Rates determined with SPECFIT using a global analysis model: A → B → C under noncatalytic conditions and A → B → C → D under catalytic conditions. [e] Rates determined with SPECFIT using single-wavelength kinetics (440 nm) fitted to one (noncatalytic conditions) or two concurrent exponentials (catalytic conditions) except the L-Arg-saturated saNOS kinetics that had to be fitted to two exponentials. [f] Not determined. [g] Minor fraction that seems to autoxidize at a rate similar to that of L-Arg-free saNOS that suggests that a small fraction of the protein may have been free of substrate.

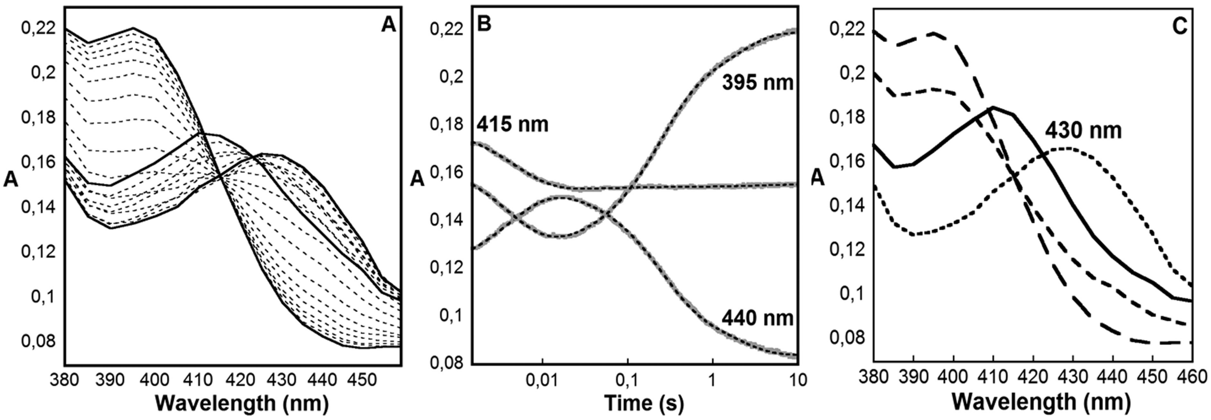

Figure 3. Kinetics of formation and decay of the transient oxygenated complex of W56H in the presence of L-Arg and H_4B (catalytic condition). (A) Set of the original optical spectra recorded after the reduced W56H had been mixed with O_2 that show the spectral transitions over a time course of 10 s. (B) Original data and fits obtained from the global analysis to the four-state kinetic model (A > B > C > D) that show the disappearance of reduced W56H (415 nm), the formation and decay of the oxygenated complex (440 nm), and the buildup of the ferric state as the reaction is completed (395 nm). (C) Calculated optical absorption spectra of the reduced (state A, solid line), oxygenated (state B, dotted line), and ferric (states C and D, dashed lines) forms.

variants displayed apparent rates of formation of the $Fe^{II}O_2$ complex [k_{obs} (Table 2)] and bimolecular rate constants [k_{on} (Table 2)] similar to those of WT saNOS[45] (Table 2). As was observed previously for WT saNOS, the rates of formation of the oxygenated complex were not sensitive to the presence of the pterin[45] (Table 2).

The rates of decay of $Fe^{II}O_2$ [k_{obs} (Table 2)] through either autoxidation [$k_{decay}(H_2B)$] or activation [$k_{decay}(H_4B)$] were obtained by a combination of global and single-wavelength analyses. Under noncatalytic conditions, the autoxidation rate of the $Fe^{II}O_2$ complex of WT saNOS saturated with L-Arg and H_2B was 0.86 s^{-1} (Table 2). This autoxidation rate was 5-fold slower for W56H (0.17 s^{-1}), while W56F (5.6 s^{-1}) and W56Y (17.2 s^{-1}) exhibited autoxidation rates 5−17-fold higher than that of WT saNOS (Table 2). Similarly, the autoxidation rate of L-Arg-bound but pterin-free samples was smaller for W56H (0.33 s^{-1}) than that of WT saNOS (1.6 s^{-1}) but higher for W56F and W56Y variants [9.7 and 27.9 s^{-1}, respectively (Table 2)]. The stopped-flow kinetics thus showed that the rate of decay of the $Fe^{II}O_2$ complex through autoxidation increases in

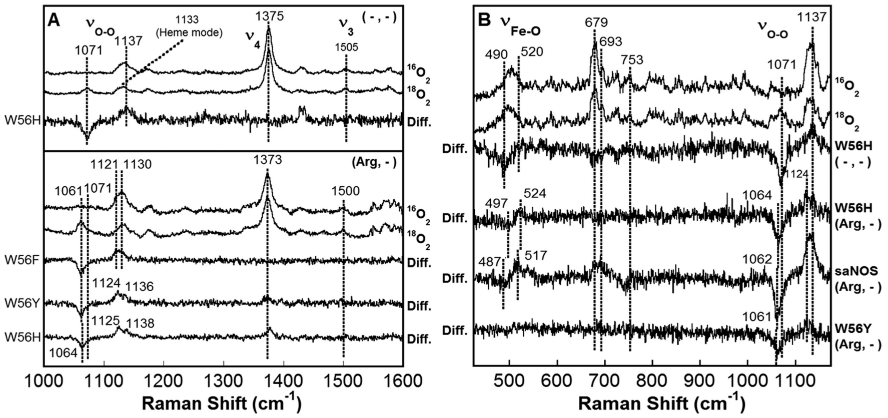

Figure 4. High-frequency (A) and low-frequency (B) regions of the resonance Raman spectra of the oxygenated complexes ($Fe^{II}O_2$) of the W56 variants. (A) The top panel shows the high-frequency region (900−1600 cm^{-1}) of the resonance Raman spectra of W56H with $^{16}O_2$ and $^{18}O_2$ in the absence of L-Arg. The difference spectrum is the $^{16}O_2$ minus $^{18}O_2$ spectrum. The bottom panel shows the high-frequency region of the resonance Raman spectra of W56F with $^{16}O_2$ and $^{18}O_2$ in the presence of L-Arg. The difference spectra are the $^{16}O_2$ minus $^{18}O_2$ spectra of all three L-Arg-bound W56 variants. (B) Low-frequency region (400−1200 cm^{-1}) of the resonance Raman spectra of W56H with $^{16}O_2$ and $^{18}O_2$ in the absence of L-Arg. The difference spectra are the $^{16}O_2$ minus $^{18}O_2$ spectra in the absence (−, −) (W56H) and presence of L-Arg (Arg, −) (W56H, WT saNOS, and W56Y). The spectrum of WT saNOS is shown as a reference.

the following order: W56H < WT < W56F < W56Y. These results are consistent with those of Tejero et al. with the W188H variant of iNOS.[47]

In contrast to the rates of decay measured with L-Arg- and H_2B-bound samples, those obtained with L-Arg- and H_4B-bound samples could not be fitted with a single exponential. The transition of the $Fe^{II}O_2$ complex to the ferric state had to be fitted to two exponentials either by global analysis [sequential model (Table 2)] or by single-wavelength kinetics with a concurrent (Table 2) and sequential model (not shown). These methods gave similar rates. The slower rate (that corresponds to small amplitude changes) seems to correspond to a fraction of the $Fe^{II}O_2$ complex undergoing autoxidation [$k_{decay}(H_2B)$]. Indeed, this rate is similar to that determined in the presence of H_2B and shows the same trend: W56H < WT < W56F < W56Y. The faster rate that corresponds to the rate of O_2 activation and catalysis [$k_{decay}(H_4B)$] seems to obey the same rule; the $k_{decay}(H_4B)$ of W56H was 5-fold slower (4.1 s^{-1}) than that of WT saNOS (22.6 s^{-1}). In contrast, the $k_{decay}(H_4B)$ values of W56F (69.7 s^{-1}) and W56Y (87.7 s^{-1}) were 3−4-fold faster (Table 2). This trend is nicely illustrated in Figure S5 of the Supporting Information, which compares the lifetime of the transient $Fe^{II}O_2$ complexes of WT saNOS with that of its W56 variants (calculated from the global analysis). One can notice that even though the formation of $Fe^{II}O_2$ occurs at a similar pace, its fate differs as a result of the mutations introduced at position 56. The complex is long-lived for W56H and short-lived for W56Y and W56F compared to WT saNOS. The ratio of $k_{decay}(H_4B)$ to $k_{decay}(H_2B)$ reveals the H_4B-induced catalysis. This ratio, 24−26 for WT saNOS and W56H, is similar in amplitude to those of other NOSs.[18,20] This ratio is, however, smaller for W56F (ratio of 12) and W56Y (ratio of 5), which suggests that the oxygenated complex was less efficiently activated by H_4B in these variants (see Discussion).

Resonance Raman Spectroscopy of the $Fe^{II}O_2$ Complexes of the W56 Variants. We also used resonance Raman spectroscopy to determine if the W56 mutations had an impact on the frequencies of the Fe−OO (ν_{Fe-OO}) and O−O (ν_{O-O}) stretching modes. The resonance Raman spectra were recorded using a homemade continuous-flow mixer[45] when the oxygenated complex had reached its maximal concentration as determined from the stopped-flow kinetics. Those of substrate-free W56F and W56Y could not be obtained as fast rates of autoxidation prevented the accumulation of the $Fe^{II}O_2$ complex (not shown). In contrast, the buildup of the $Fe^{II}O_2$ complex was observed for all variants in the presence of L-Arg. Figure 4A displays the high-frequency region of the resonance Raman spectra of the $Fe^{II}O_2$ complex of the W56 variants. The ν_4 and ν_3 lines of the W56 variants that indicate the oxidation and coordination state of the heme, respectively, are similar to those obtained for WT saNOS by Chartier et al.[45] In the absence of L-Arg (Figure 4A, top panel), W56H exhibited a ν_4 line at 1375 cm^{-1} and a ν_3 line at 1505 cm^{-1}, while in the presence of the substrate, all W56 variants exhibited a ν_4 line at 1373 cm^{-1} and a ν_3 line at 1500 cm^{-1} (Figure 5A, bottom panel). These heme vibrationnal modes are typical for a six-coordinate and low-spin $Fe^{II}O_2$ complex.

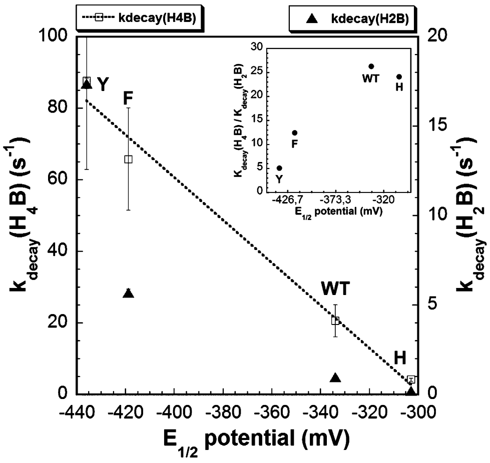

Figure 5. Plots of the rates of O_2 activation [$k_{decay}(H_4B)$] and autoxidation of the oxygenated complex [$k_{decay}(H_2B)$] as a function of the heme midpoint redox potential ($E_{1/2}$). $k_{decay}(H_4B)$ decreases linearly as $E_{1/2}$ increases ($R^2 = 0.99$), while $k_{decay}(H_2B)$ decreases more abruptly. The plot of the $k_{decay}(H_4B)/k_{decay}(H_2B)$ ratios (inset) vs $E_{1/2}$ indicates that the optimal ratio is reached near −350 mV.

An isotope sensitive line centered near 1135 cm^{-1} (1071 cm^{-1} with $^{18}O_2$) was detected in the high-frequency region of the resonance Raman spectra of all substrate-bound W56 variants (Figure 4A, bottom panel) and for substrate-free W56H (Figure 4A, top panel). It was assigned to the O−O stretching mode (ν_{O-O}) on the basis of the frequency and amplitude of the isotopic shift that are similar to those of WT saNOS (Table 3). It must be pointed out that there is no ambiguity in the assignment of the O−O frequencies of substrate-free W56H. In the absence of L-Arg, a single line at 1137 cm^{-1} shifts to 1071 cm^{-1} with $^{18}O_2$ (Figure 4A, top panel, and Figure S6 of the Supporting Information). The amplitude of the isotopic shift (66 cm^{-1}) fits the expected value of 65 cm^{-1} for a diatomic oscillator, and the ν_{O-O} frequency of W56H is identical to that of WT saNOS (Table 3). However, the assignment of the frequency of the ν_{O-O} mode of the substrate-bound variants is made difficult by vibrational coupling of the ν_{O-O} mode obtained with $^{16}O_2$ with an overlapping heme mode centered at 1133 cm^{-1} as observed previously with WT saNOS.[45] This effect is similar to that observed for adamantanone-bound cytochrome P450cam in which a substrate mode with an energy similar to that of the ν_{O-O} mode caused a broadening of the O−O stretching mode region with $^{16}O_2$ compared to that with $^{18}O_2$.[62] For L-Arg-bound WT saNOS, this vibrational coupling was apparent from the regression analysis of the lines of the O−O region with $^{16}O_2$ and $^{18}O_2$ as the relative intensities and line widths with $^{16}O_2$ differed from those with $^{18}O_2$.[45] This vibrational coupling likely explains why the line shape with $^{18}O_2$ in the O−O region (near 1064 cm^{-1}) was similar in all spectra while differences are observed in the relative intensities of lines in the O−O region with $^{16}O_2$ (near 1135 cm^{-1}) (Figure 4A, bottom panel). Apparently because of this vibrational coupling, the frequencies of the ν_{O-O} modes with $^{16}O_2$ could not be obtained reliably with the W56 variants by regression analysis (not shown). Therefore, only the ν_{O-O} frequencies obtained with $^{18}O_2$ were used for comparison. In the presence of L-Arg (Figure 4A, bottom panel), all three W56 variants exhibited two isotope sensitive lines, like WT saNOS.[45] The higher-frequency mode, similar to the ν_{O-O} mode observed for L-Arg-free saNOS, displays a frequency that is 2 cm^{-1} lower (for W56F and W56Y) and 1 cm^{-1} higher (for W56H) than that observed for WT saNOS [1075 cm^{-1} (Table 3 and Figure S7 of the Supporting Information)]. Similarly and most importantly, the lower-frequency mode, arising as L-Arg and the terminal oxygen of the heme-bound O_2 form a hydrogen bond interaction, has a frequency that is 1 cm^{-1} lower (for W56F and W56Y) and 2 cm^{-1} higher (for W56H) than that of WT saNOS [found at 1062 cm^{-1} (Table 3 and Figure S7 of the Supporting Information)]. Overall, the ν_{O-O} frequencies of the L-Arg-bound W56 variants decrease in the following order: W56H > WT > W56Y ∼ W56F (Table 2 and Figure S7 of the Supporting Information).

Table 3. Frequencies of the ν_{Fe-OO} and ν_{O-O} Modes of the W56 Variants with and without L-Arg

protein	condition	ν_{Fe-OO} ($^{18}O_2$)[a] (cm^{-1})	ν_{O-O} ($^{18}O_2$)[b] (cm^{-1})	ref
saNOS WT	(−, −)	517 (487)	(1071)	45
	(Arg, −)	517 (487)	(1062, 1074.5)	45
W56F	(−, −)	ND[c]	ND[c]	this work
	(Arg, −)	undetectable	(1061, 1073)	this work
W56Y	(−, −)	ND[c]	ND[c]	this work
	(Arg, −)	undetectable	(1061, 1072)	this work
W56H	(−, −)	520 (490)	(1071)	this work
	(Arg, −)	524 (497)	(1064, 1075.5)	this work

[a] The ν_{Fe-OO} frequencies are those obtained from the $^{16}O_2$ minus $^{18}O_2$ difference spectra. [b] A regression analysis of the O−O mode was performed with a mixed Lorentzian/Gaussian function without any restrictions in terms of frequency, width at half-height, or Lorentzian/Gaussian ratio using Grams. Values in this table are those obtained from the regression analysis with the $^{18}O_2$ spectra. Those with $^{16}O_2$ are not considered reliable because the O−O mode overlaps a heme mode causing vibrational coupling of these modes. [c] Not determined as the oxygenated complex did not accumulate as determined from the stopped-flow kinetics.

In the low-frequency region of the resonance Raman spectra (400−1200 cm^{-1}), the Fe−OO stretching mode (ν_{Fe-OO}) of substrate-free W56H was detected in the $^{16}O_2$ minus $^{18}O_2$ difference spectrum (Figure 4B). An isotope sensitive line centered around 520 cm^{-1} (490 cm^{-1} with $^{18}O_2$) was detected and assigned to the Fe−OO stretching mode (ν_{Fe-OO}) of W56H on the basis of the frequency and amplitude of its isotope shift (Figure 4B). With respect to that of WT saNOS, ν_{Fe-OO} of W56H is upshifted by ∼3 cm^{-1}, thus indicating an increase of the strength of the Fe−O bond (Table 3). With L-Arg-bound W56H, the ν_{Fe-OO} mode was upshifted by 7 cm^{-1} to 524 cm^{-1} (Figure 4B and Table 3). It must be pointed out that the Fe−O bond strength of oxygenated complexes of model compounds shows a direct correlation with the strength of the axial ligand; i.e., the stronger the axial ligand, the stronger the Fe−O bond.[63] However, the opposite trend is observed in heme proteins.[63] For example, cytochrome P450cam with a strong thiolate ligand displays much lower ν_{Fe-O} frequencies compared to those of histidine-coordinated heme proteins.[62] Thus, the apparent 3−7 cm^{-1} upshift of ν_{Fe-OO} for the W56H variant is consistent with the decreased electronic density of the thiolate that is suggested by the 2 cm^{-1} upshift of ν_{O-O} (Table 3). We tried without success to determine the frequency of ν_{Fe-OO} of W56F and W56Y saturated with L-Arg. The $^{16}O_2$ minus $^{18}O_2$ difference spectra recorded in the low-frequency region did not show any isotope sensitive line in the ν_{Fe-OO} region [W56Y (Figure 4B)]. The smaller amount of the $Fe^{II}O_2$ complex that accumulates during the course of the reaction (Figure S5 of the Supporting Information), the intrinsic weak intensity of the ν_{Fe-OO} line and the poor quality of the resonance Raman spectra for these variants likely contributed to this situation.

■ DISCUSSION

The conserved tryptophan residue of NOSs (W56 in saNOS) forms π−π stacking interactions with the heme and supplies a side chain hydrogen bond from its indole nitrogen to the proximal cysteinate sulfur (C62 in saNOS), which helps to stabilize the negative charge of the deprotonated sulfur of the proximal cysteine.[35,36,40,55,64,65] The purpose of this study was to investigate how the modification of this hydrogen bonding interaction, which modulates the electronic density of the proximal cysteine, affects the enzymatic activity of a NOS. The characterization of W56 variants of saNOS designed to decrease (W56H) or increase (W56F and W56Y) the electron density of the proximal cysteine establishes a direct correlation between the strength of the Trp−Cys hydrogen bond and its effect on (1) σ-bonding and π-backbonding of the heme with a distal ligand (CO, •NO, and most importantly O_2), (2) the redox potential of NOS heme, and (3) the catalytic functioning of NOS, including O_2 activation and autoxidation.

Conservation of the Overall Structure and the Distal Environment of the Heme. It is first necessary to verify the structural integrity of the heme environment of the W56 variants. For that purpose, we can analyze the effects on the heme spectral fingerprints as the substrate L-Arg forms the electrostatic and/or steric interactions with heme ligands that are revealed by resonance Raman spectroscopy (reviewed in ref 59). We observe here that the $Fe^{II}CO$ complexes of all W56 variants show the same sensitivity to L-Arg binding that is probed by the restriction of the conformational freedom: diminution of the number of conformations, narrowing of the line width, and upshift in the δ_{Fe-C-O} frequency (Table 1). Besides, the frequency of the δ_{Fe-C-O} mode in the presence of L-Arg remains almost identical (~565 cm^{-1}) for all three W56 variants, suggesting the maintenance of the $Fe^{II}CO$ geometry.[66] As previously observed with WT saNOS, the ν_{O-O} frequency decreased in all three W56 variants upon L-Arg binding (Table 3 and Figure S7 of the Supporting Information), which is an indication that similar hydrogen bonding interactions are formed with the terminal oxygen of the heme-bound O_2.[45] In terms of its effect on kinetics, L-Arg diminishes the rate of autoxidation of the oxygenated complex for all W56 variants as with WT saNOS (Table 2 and Table S1 of the Supporting Information). In addition to these L-Arg-induced effects, the similar frequencies of the high- and low-frequency heme modes obtained in various states [Fe^{III}, Fe^{II}, and $Fe^{II}CO$ (Table S2 of the Supporting Information)] suggest a conservation of the overall heme structure.

Mutations at Position 56 of saNOS Affect σ- and π-Bonding with O_2 and CO. The investigations of the role of the proximal Trp on the coordination of distal ligands have so far focused on noncatalytic ligands (such as CO or •NO[35,36,40]) or concerned only the F/Y mutants of eNOS and nNOS[36−40] or only the H variant of iNOS.[47] The comparative analysis of this effect for the complete set of variants (F, Y, and H) within the same protein framework reported here reveals two opposite trends. On one hand, the W56F and W56Y variants display reduced ν_{Fe-CO} and ν_{O-O} frequencies consistent with an increased electron density of the thiolate in the absence of the Trp−Cys hydrogen bond. On the other hand, the upshifts of ν_{Fe-CO} and ν_{Fe-OO} for the W56H variant suggest that the electronic density of the thiolate decreased as a His−Cys hydrogen formed and that it is stronger than the Trp−Cys hydrogen bond of WT saNOS. This strong hydrogen bond likely accounts for the enhanced σ-bonding with the distal ligands and weakened π-backbonding of the heme Fe with CO and O_2 (Tables 1 and 3). Together, W56F, W56Y, and W56H of saNOS constitute a set of variants with increased thiol basicity (W56F and W56Y) or decreased thiol basicity (W56H) that modulate σ-bonding and π-backbonding with CO and O_2.

Effect of the W56 Mutations on O_2 Binding and Catalysis. L-Arg hydroxylation by NOSs proceeds via the initial formation of a $Fe^{II}O_2$ complex. Its activation necessitates the transfer of an electron from H_4B and may proceed via a "push−pull" effect[31] to a compound I species defined as a ferryl heme with an associated radical. The hydrogen bonds among L-Arg, water, and the terminal oxygen atom of the heme-bound O_2 exert the "pull effect" that may favor the double protonation of the terminal oxygen, while electron density of the proximal cysteine would provide a push effect. Both effects would promote the cleavage of the O−O bond and help activate the heme-bound O_2.[2,26,45,59,67] We show here that the push effect that is modulated in W56 variants has a strong impact on the rate of decay of the $Fe^{II}O_2$ complex. When the proximal cysteinate is less rich in electrons, as in the W56H variant, $k_{decay}(H_4B)$ and $k_{decay}(H_2B)$ are 3−5-fold smaller than that of WT saNOS (Table 2 and Table S1 of the Supporting Information). On the other hand, when the electron density of the cysteinate is increased, as with the W56F and W56Y variants, $k_{decay}(H_4B)$ and $k_{decay}(H_2B)$ are 3−17-fold larger (Table 2 and Table S1 of the Supporting Information). We did not observe any effect of the W56 mutation on the reaction sequence of O_2 activation. Each variant exhibited a 5−24-fold enhancement of the rate of O_2 activation by H_4B (Table 2). The amplitude of the enhancement by H_4B with W56H is similar to that of WT saNOS and those of other bacterial NOS. However, this ratio is lower for W56F and W56Y, which reveals that the oxygenated complex was less efficiently activated by H_4B in these variants and suggests a competition between decay of the oxygenated complex via autoxidation and via catalysis. Tejero et al.[47] revealed that the rates of activation of O_2 and hydroxylation of L-Arg are reduced for the W188H variant of iNOSox. In addition, they detected a new catalytic intermediate in the single-turnover reaction with L-Arg. Although we observed a reduction of the rate of O_2 activation with W56H saNOS as they reported with W188H iNOS, we did not detect this intermediate whose nature remains to be determined.

The Heme Midpoint Reduction Potential Is Sensitive to the NH···S^- Hydrogen Bond Interaction of W56. The W56 variants of saNOS show that within the same protein framework, mutations of the conserved Trp of NOS can effectively change positively (W56H) and negatively (W56F and W56Y) the heme midpoint potential. Besides, the catalytic activity of heme proteins appears closely linked to $E_{1/2}$ as $k_{decay}(H_4B)$ and $k_{decay}(H_2B)$ seem to vary with the heme redox potential.[47,57] This relationship is illustrated in Figure 5 for the saNOS variants. As $E_{1/2}$ increases, both $k_{decay}(H_2B)$ and $k_{decay}(H_4B)$ become smaller. These results extend those obtained with iNOS by Stuehr's group, who observed a 6-fold reduction in the rate of O_2 activation for the W188H variant that was related to the 88 mV increase in its $E_{1/2}$ potential,[47] and those of Ost et al., who showed using variants at position F393 of $P450_{BM3}$ a direct correlation between an increased stability of heme−O_2 species versus autoxidation and an increase in $E_{1/2}$.[57,68,69] Modifications to the electronic structure of the heme (through distortion of the porphyrin or the addition of substituents), the heme ligation and spin state, and the polarity of the heme binding pocket could modulate the heme redox potential.[70−74] However, we can essentially rule out these possibilities for saNOS: as the interactions between L-Arg and CO and O_2 are not modified by the mutations introduced at position W56 of saNOS, there is no evidence that the polarity of the heme binding pocket has changed upon mutation of W56. The hemes of the W56 variants and WT saNOS remain five-coordinate and high-spin in the ferric state in the presence of the substrate L-Arg. Finally, as discussed above, the similar frequencies of several heme modes in various heme states suggest the conservation of the heme environment

(Table S2 of the Supporting Information). On the other hand, various model compounds of P450cam, CPO, and iron−sulfur proteins, designed to vary the electron density of a Fe-coordinated sulfur atom through the formation of the NH···S^- bond, showed that as the electron density of the sulfur decreases, the $E_{1/2}$ potential increases.[75−77] This is the conclusion that is reached here with the W56 variants. The decreased midpoint redox potential of W56F and W56Y variants arises from the absence of the indole NH···S^- hydrogen bond. On the other hand, the increased heme redox potential of the W56H variant arises from the formation of a strong His56···Cys62 hydrogen bond. Together, the W56 variants show in a protein system that the heme redox potential may be modulated by the addition or removal of hydrogen bonding interactions involving the proximal cysteine with a direct impact on $k_{decay}(H_4B)$ and $k_{decay}(H_2B)$. We also notice that the modification of $E_{1/2}$ has a larger impact on $k_{decay}(H_2B)$ (nonlinear response) than on $k_{decay}(H_4B)$ (Figure 5). The apparently less efficient activation of the oxygenated complex of W56F and W56Y at low $E_{1/2}$ values may arise as $k_{decay}(H_2B)$ increased rapidly and approached $k_{decay}(H_4B)$. A plot of the $k_{decay}(H_4B)/k_{decay}(H_2B)$ ratios as a function of $E_{1/2}$ reveals that the maximal value is reached around −350 mV, which is close to the value of WT saNOS (inset of Figure 5). It thus appears that the increased rate of O_2 activation of W56F and W56Y may come at the price of an increased rate of autoxidation. With regard to WT saNOS, these results suggest that the Trp56···Cys62 hydrogen bond interaction is important to dampen the push effect, which effectively reduces the rate of autoxidation enough to allow O_2 activation by H_4B while maintaining a relatively fast catalytic rate during the first catalytic cycle. In addition, the Trp56···Cys62 hydrogen bond increases $E_{1/2}$ by ∼90 mV to values within the range expected for heme reduction of saNOS from NADPH via a reductase in a physiological context.

CONCLUSIONS

We report here an investigation of the impact of the modulation of the thiolate basicity on the kinetic and spectroscopic properties of the oxygenated complex of saNOS. The formation of the NH···S^- hydrogen bond from H56 of the W56H variant caused an upshift in both ν_{Fe-CO} and ν_{Fe-OO} showing that the decreased electron density of the proximal cysteinate, as it weakened the Fe−S^- bond, enhanced σ-bonding with CO and O_2. The decreased thiolate density also caused a weakening of π-backbonding with CO and O_2. These effects on σ-bonding and π-backbonding of W56H with exogenous ligands are the opposite of those displayed by the W56F and W56Y variants that have no NH···S^- hydrogen bond. The redox potentiometry measurement of the W56 variants clearly demonstrates that as the electron density of the thiolate is increased by removing the NH···S^- hydrogen bond (W56F and W56Y variants), this led to an increase in the push effect, as $k_{decay}(H_4B)$ and $k_{decay}(H_2B)$ are both increased. However, the increase is much more pronounced for $k_{decay}(H_2B)$ than for $k_{decay}(H_4B)$. It thus appears that in NOS, in addition to its recognized role in maintaining the integrity of the thiolate bond, the conserved tryptophan···cysteinate hydrogen bond is necessary to dampen the push effect and to optimize catalysis by preserving a relatively fast rate of O_2 activation while sufficiently reducing the rate of autoxidation of the $Fe^{II}O_2$ complex to maintain an efficient activation of the oxygenated complex by H_4B during the L-Arg hydroxylation reaction.

ASSOCIATED CONTENT

Supporting Information

Rates of formation and decay of the oxygenated complex of saNOS and its W56 variants in the absence of L-Arg (Table S1), heme mode frequencies in the low- and high-frequency regions of the reduced (Fe^{II}), ferric (Fe^{III}), and $Fe^{II}CO$ forms of saNOS and the W56 variants saturated with L-Arg (Table S2), affinities of ferric saNOS and its W56 variants for the substrate L-Arg (Table S3), crystallographic structure of saNOS highlighting the active site and the interactions between the heme Fe and the sulfur of C62 (Fe−Cys bond) and between the proximal W56 and C62 (NH···S^- hydrogen bond) (Figure S1), titration curves of ferric saNOS and the W56H variant as a function of L-Arg concentration (Figure S2), titration curves of ferric, imidazole-bound saNOS (A), W56H (B), W56F (C), and W56Y (D) (1 mM imidazole) as a function of L-Arg concentration (Figure S3), calculated spectra of the reduced, oxygenated, and ferric states obtained from global analysis of kinetic data recorded under catalytic conditions (Arg, H_4B) for saNOS, W56F, and W56Y (Figure S4), lifetime of the transient oxygenated complex of saNOS and the W56 variants formed after the reduced enzymes had been mixed with O_2 under catalytic conditions (L-Arg, H_4B) (Figure S5), regression analyses of the O−O stretching mode region of the $^{16}O_2$ minus $^{18}O_2$ difference resonance Raman spectra of L-Arg-free WT saNOS and the W56H variant (Figure S6), and regression analyses of the O−O stretching mode region of the $^{18}O_2$ resonance Raman spectra of L-Arg-bound WT saNOS and all three W56 variants (Figure S7). This material is available free of charge via the Internet at http://pubs.acs.org.

AUTHOR INFORMATION

Corresponding Author

*Département de biochimie, de microbiologie et de bio-informatique, PROTEO and IBIS, pavillon Charles-Eugène Marchand, room 3163, Université Laval, Québec, Canada G1V 0A6. Telephone: (418) 656-2131, ext. 13515. Fax: (418) 656-7176. E-mail: manon.couture@bcm.ulaval.ca.

Funding

This work was supported by NSERC Discovery Grant 250073 and CFI Grant 7128 to M.C.

ABBREVIATIONS

NOS, nitric oxide synthase; NO, nitric oxide; L-Arg, L-arginine; H_4B, (6*R*)-5,6,7,8-tetrahydro-L-biopterin; H_2B, 7,8-dihydro-L-biopterin; saNOS, nitric oxide synthase-like protein from *S. aureus*; bsNOS, nitric oxide synthase-like protein from *B. subtilis*; iNOS, inducible nitric oxide synthase; nNOS, neuronal nitric oxide synthase; eNOS, endothelial nitric oxide synthase; Fe^{III}, ferric state of iron; Fe^{II}, reduced state of iron; $Fe^{II}CO$, carbon monoxide complex; $Fe^{II}O_2$, oxygenated complex; WT, wild-type; NHE, normal hydrogen electrode.

REFERENCES

(1) Alderton, W. K., Cooper, C. E., and Knowles, R. G. (2001) Nitric oxide synthases: Structure, function and inhibition. *Biochem. J.* *357*, 593−615.

(2) Li, H., and Poulos, T. L. (2005) Structure-function studies on nitric oxide synthases. *J. Inorg. Biochem.* *99*, 293−305.

(3) Gorren, A. C., and Mayer, B. (2007) Nitric-oxide synthase: A cytochrome P450 family foster child. *Biochim. Biophys. Acta 1770*, 432−445.

(4) Stuehr, D. J. (1999) Mammalian nitric oxide synthases. *Biochim. Biophys. Acta 1411*, 217−230.

(5) Daff, S., Noble, M. A., Craig, D. H., Rivers, S. L., Chapman, S. K., Munro, A. W., Fujiwara, S., Rozhkova, E., Sagami, I., and Shimizu, T. (2001) Control of electron transfer in neuronal NO synthase. *Biochem. Soc. Trans. 29*, 147−152.

(6) Stuehr, D. J., Tejero, J., and Haque, M. M. (2009) Structural and mechanistic aspects of flavoproteins: Electron transfer through the nitric oxide synthase flavoprotein domain. *FEBS J. 276*, 3959−3974.

(7) Stuehr, D. J. (1997) Structure-function aspects in the nitric oxide synthases. *Annu. Rev. Pharmacol. Toxicol. 37*, 339−359.

(8) Crane, B. R., Sudhamsu, J., and Patel, B. A. (2010) Bacterial nitric oxide synthases. *Annu. Rev. Biochem. 79*, 445−470.

(9) Sudhamsu, J., and Crane, B. R. (2009) Bacterial nitric oxide synthases: What are they good for? *Trends Microbiol. 17*, 212−218.

(10) Crane, B. R. (2008) The enzymology of nitric oxide in bacterial pathogenesis and resistance. *Biochem. Soc. Trans. 36*, 1149−1154.

(11) Crane, B. R., Arvai, A. S., Ghosh, D. K., Wu, C., Getzoff, E. D., Stuehr, D. J., and Tainer, J. A. (1998) Structure of nitric oxide synthase oxygenase dimer with pterin and substrate. *Science 279*, 2121−2126.

(12) Bird, L. E., Ren, J., Zhang, J., Foxwell, N., Hawkins, A. R., Charles, I. G., and Stammers, D. K. (2002) Crystal structure of SANOS, a bacterial nitric oxide synthase oxygenase protein from *Staphylococcus aureus*. *Structure 10*, 1687−1696.

(13) Pant, K., Bilwes, A. M., Adak, S., Stuehr, D. J., and Crane, B. R. (2002) Structure of a Nitric Oxide Synthase Heme Protein from *Bacillus subtilis*. *Biochemistry 41*, 11071−11079.

(14) Sudhamsu, J., and Crane, B. R. (2006) Structure and reactivity of a thermostable prokaryotic nitric-oxide synthase that forms a long-lived oxy-heme complex. *J. Biol. Chem. 281*, 9623−9632.

(15) Crane, B. R., Arvai, A. S., Gachhui, R., Wu, C., Ghosh, D. K., Getzoff, E. D., Stuehr, D. J., and Tainer, J. A. (1997) The structure of nitric oxide synthase oxygenase domain and inhibitor complexes. *Science 278*, 425−431.

(16) Gusarov, I., Starodubtseva, M., Wang, Z. Q., McQuade, L., Lippard, S. J., Stuehr, D. J., and Nudler, E. (2008) Bacterial nitric-oxide synthases operate without a dedicated redox partner. *J. Biol. Chem. 283*, 13140−13147.

(17) Agapie, T., Suseno, S., Woodward, J. J., Stoll, S., Britt, R. D., and Marletta, M. A. (2009) NO formation by a catalytically self-sufficient bacterial nitric oxide synthase from *Sorangium cellulosum*. *Proc. Natl. Acad. Sci. U.S.A. 106*, 16221−16226.

(18) Adak, S., Aulak, K. S., and Stuehr, D. J. (2002) Direct evidence for nitric oxide production by a nitric-oxide synthase-like protein from *Bacillus subtilis*. *J. Biol. Chem. 277*, 16167−16171.

(19) Adak, S., Bilwes, A. M., Panda, K., Hosfield, D., Aulak, K. S., McDonald, J. F., Tainer, J. A., Getzoff, E. D., Crane, B. R., and Stuehr, D. J. (2002) Cloning, expression, and characterization of a nitric oxide synthase protein from *Deinococcus radiodurans*. *Proc. Natl. Acad. Sci. U.S.A. 99*, 107−112.

(20) Reece, S. Y., Woodward, J. J., and Marletta, M. A. (2009) Synthesis of nitric oxide by the NOS-like protein from *Deinococcus radiodurans*: A direct role for tetrahydrofolate. *Biochemistry 48*, 5483−5491.

(21) Johnson, E. G., Sparks, J. P., Dzikovski, B., Crane, B. R., Gibson, D. M., and Loria, R. (2008) Plant-pathogenic *Streptomyces* species produce nitric oxide synthase-derived nitric oxide in response to host signals. *Chem. Biol. 15*, 43−50.

(22) Shatalin, K., Gusarov, I., Avetissova, E., Shatalina, Y., McQuade, L. E., Lippard, S. J., and Nudler, E. (2008) *Bacillus anthracis*-derived nitric oxide is essential for pathogen virulence and survival in macrophages. *Proc. Natl. Acad. Sci. U.S.A. 105*, 1009−1013.

(23) Patel, B. A., Moreau, M., Widom, J., Chen, H., Yin, L., Hua, Y., and Crane, B. R. (2009) Endogenous nitric oxide regulates the recovery of the radiation-resistant bacterium *Deinococcus radiodurans* from exposure to UV light. *Proc. Natl. Acad. Sci. U.S.A. 106*, 18183−18188.

(24) Gusarov, I., and Nudler, E. (2005) NO-mediated cytoprotection: Instant adaptation to oxidative stress in bacteria. *Proc. Natl. Acad. Sci. U.S.A. 102*, 13855−13860.

(25) Gusarov, I., Shatalin, K., Starodubtseva, M., and Nudler, E. (2009) Endogenous nitric oxide protects bacteria against a wide spectrum of antibiotics. *Science 325*, 1380−1384.

(26) Pant, K., and Crane, B. R. (2006) Nitrosyl-heme structures of *Bacillus subtilis* nitric oxide synthase have implications for understanding substrate oxidation. *Biochemistry 45*, 2537−2544.

(27) Cho, K.-B., and Gauld, J. W. (2005) Second half-reaction of the nitric oxide synthase: Computational insights into the initial step and key proposed intermediate. *J. Phys. Chem. B 109*, 23706−23714.

(28) Cho, K.-B., and Gauld, J. W. (2004) Quantum chemical calculations of the NHA bound nitric oxide synthase active site: O_2 binding and implications for the catalytic mechanism. *J. Am. Chem. Soc. 126*, 10267−10270.

(29) Li, H., Igarashi, J., Jamal, J., Yang, W., and Poulos, T. L. (2006) Structural studies of constitutive nitric oxide synthases with diatomic ligands bound. *J. Biol. Inorg. Chem. 11*, 753−768.

(30) Davydov, R., Sudhamsu, J., Lees, N. S., Crane, B. R., and Hoffman, B. M. (2009) EPR and ENDOR characterization of the reactive intermediates in the generation of NO by cryoreduced oxy-nitric oxide synthase from *Geobacillus stearothermophilus*. *J. Am. Chem. Soc. 131*, 14493−14507.

(31) Santolini, J. (2011) The molecular mechanism of mammalian NO-synthases: A story of electrons and protons. *J. Inorg. Biochem. 105*, 127−141.

(32) Zhu, Y., and Silverman, R. B. (2008) Revisiting heme mechanisms. A perspective on the mechanisms of nitric oxide synthase (NOS), heme oxygenase (HO) and cytochrome P450s (CYP450s). *Biochemistry 47*, 2231−2243.

(33) Auclair, K., Moenne-Loccoz, P., and Ortiz de Montellano, P. R. (2001) Roles of the proximal heme thiolate ligand in cytochrome p450(cam). *J. Am. Chem. Soc. 123*, 4877−4885.

(34) Yoshioka, S., Takahashi, S., Ishimori, K., and Morishima, I. (2000) Roles of the axial push effect in cytochrome P450cam studied with the site-directed mutagenesis at the heme proximal site. *J. Inorg. Biochem. 81*, 141−151.

(35) Brunel, A., Wilson, A., Henry, L., Dorlet, P., and Santolini, J. (2011) The proximal hydrogen bond network modulates *Bacillus subtilis* nitric-oxide synthase electronic and structural properties. *J. Biol. Chem. 286*, 11997−12005.

(36) Lang, J., Driscoll, D., Gelinas, S., Rafferty, S. P., and Couture, M. (2009) Trp180 of endothelial NOS and Trp56 of bacterial saNOS modulate σ bonding of the axial cysteine to the heme. *J. Inorg. Biochem. 103*, 1102−1112.

(37) Adak, S., Crooks, C., Wang, Q., Crane, B. R., Tainer, J. A., Getzoff, E. D., and Stuehr, D. J. (1999) Tryptophan 409 controls the activity of neuronal nitric-oxide synthase by regulating nitric oxide feedback inhibition. *J. Biol. Chem. 274*, 26907−26911.

(38) Adak, S., and Stuehr, D. J. (2001) A proximal tryptophan in NO synthase controls activity by a novel mechanism. *J. Inorg. Biochem. 83*, 301−308.

(39) Adak, S., Wang, Q., and Stuehr, D. J. (2000) Molecular basis for hyperactivity in tryptophan 409 mutants of neuronal NO synthase. *J. Biol. Chem. 275*, 17434−17439.

(40) Couture, M., Adak, S., Stuehr, D. J., and Rousseau, D. L. (2001) Regulation of the properties of the heme-NO complexes in nitric-oxide synthase by hydrogen bonding to the proximal cysteine. *J. Biol. Chem. 276*, 38280−38288.

(41) Wilson, D. J., and Rafferty, S. P. (2001) A structural role for tryptophan 188 of inducible nitric oxide synthase. *Biochem. Biophys. Res. Commun. 287*, 126−129.

(42) Yumoto, T., Sagami, I., Daff, S., and Shimizu, T. (2000) Roles of the heme proximal side residues tryptophan409 and tryptophan421 of neuronal nitric oxide synthase in the electron transfer reaction. *J. Inorg. Biochem. 82*, 163−170.

(43) Chartier, F. J., and Couture, M. (2004) Stability of the heme environment of the nitric oxide synthase from *Staphylococcus aureus* in the absence of pterin cofactor. *Biophys. J. 87*, 1939−1950.

(44) Chartier, F. J. M., and Couture, M. (2007) Interactions between substrates and the haem-bound nitric oxide of ferric and ferrous bacterial nitric oxide synthases. *Biochem. J. 401*, 235−245.

(45) Chartier, F. J., Blais, S. P., and Couture, M. (2006) A Weak Fe-O Bond in the Oxygenated Complex of the Nitric-oxide Synthase of *Staphylococcus aureus*. *J. Biol. Chem. 281*, 9953−9962.

(46) Chartier, F. J., and Couture, M. (2007) Substrate-specific interactions with the heme-bound oxygen molecule of nitric-oxide synthase. *J. Biol. Chem. 282*, 20877−20886.

(47) Tejero, J., Biswas, A., Wang, Z. Q., Page, R. C., Haque, M. M., Hemann, C., Zweier, J. L., Misra, S., and Stuehr, D. J. (2008) Stabilization and characterization of a heme-oxy reaction intermediate in inducible nitric oxide synthase. *J. Biol. Chem. 283*, 33498−33507.

(48) Zheng, L., Baumann, U., and Reymond, J. L. (2004) An efficient one-step site-directed and site-saturation mutagenesis protocol. *Nucleic Acids Res. 32*, e115.

(49) Appleby, C. A. (1978) Purification of *Rhizobium* cytochromes P-450. *Methods Enzymol. 52*, 157−166.

(50) Copeland, R. A. (2000) *Enzymes. A practical introduction to structure, mechanism, and data analysis*, 2nd ed., Wiley-VCH, New York.

(51) Gorren, A. C., Schmidt, K., and Mayer, B. (2002) Binding of L-arginine and imidazole suggests heterogeneity of rat brain neuronal nitric oxide synthase. *Biochemistry 41*, 7819−7829.

(52) Benson, B. B., and Krause, D. (1980) The Concentration and Isotopic Fractionation of Gases Dissolved in Fresh-Water in Equilibrium with the Atmosphere. 1. Oxygen. *Limnol. Oceanogr. 25*, 662−671.

(53) Balland, V., Hureau, C., Cusano, A. M., Liu, Y., Tron, T., and Limoges, B. (2008) Oriented immobilization of a fully active monolayer of histidine-tagged recombinant laccase on modified gold electrodes. *Chemistry 14*, 7186−7192.

(54) Giroud, C., Moreau, M., Mattioli, T. A., Balland, V., Boucher, J. L., Xu-Li, Y., Stuehr, D. J., and Santolini, J. (2010) Role of arginine guanidinium moiety in nitric-oxide synthase mechanism of oxygen activation. *J. Biol. Chem. 285*, 7233−7245.

(55) Sabat, J., Stuehr, D. J., Yeh, S. R., and Rousseau, D. L. (2009) Characterization of the proximal ligand in the P420 form of inducible nitric oxide synthase. *J. Am. Chem. Soc. 131*, 12186−12192.

(56) Suzuki, N., Higuchi, T., Urano, Y., Kikuchi, K., Uekusa, H., Ohashi, Y., Uchida, T., Kitagawa, T., and Nagano, T. (1999) Novel iron porphyrin-alkanethiolate complex with intramolecular NH···S hydrogen bond: Synthesis, spectroscopy, and reactivity. *J. Am. Chem. Soc. 121*, 11571−11572.

(57) Ost, T. W., Miles, C. S., Munro, A. W., Murdoch, J., Reid, G. A., and Chapman, S. K. (2001) Phenylalanine 393 exerts thermodynamic control over the heme of flavocytochrome P450 BM3. *Biochemistry 40*, 13421−13429.

(58) Ibrahim, M., Xu, C., and Spiro, T. G. (2006) Differential sensing of protein influences by NO and CO vibrations in heme adducts. *J. Am. Chem. Soc. 128*, 16834−16845.

(59) Rousseau, D. L., Li, D., Couture, M., and Yeh, S. R. (2005) Ligand-protein interactions in nitric oxide synthase. *J. Inorg. Biochem. 99*, 306−323.

(60) Spiro, T. G., and Wasbotten, I. H. (2005) CO as a vibrational probe of heme protein active sites. *J. Inorg. Biochem. 99*, 34−44.

(61) Moreau, M., Boucher, J. L., Mattioli, T. A., Stuehr, D. J., Mansuy, D., and Santolini, J. (2006) Differential effects of alkyl- and arylguanidines on the stability and reactivity of inducible NOS heme-dioxygen complexes. *Biochemistry 45*, 3988−3999.

(62) Hu, S., Schneider, A. J., and Kincaid, J. R. (1991) Resonance Raman studies of oxycytochrome P450cam: Effect of substrate structure on $\nu_{\text{O-O}}$ and $\nu_{\text{Fe-O}_2}$. *J. Am. Chem. Soc. 113*, 4815−4822.

(63) Oertling, W. A., Kean, R. T., Wever, R., and Babcock, G. T. (1990) Factors Affecting the Iron Oxygen Vibrations of Ferrous Oxy and Ferryl Oxo Heme-Proteins and Model Compounds. *Inorg. Chem. 29*, 2633−2645.

(64) Galinato, M. G., Spolitak, T., Ballou, D. P., and Lehnert, N. (2011) Elucidating the role of the proximal cysteine hydrogen-bonding network in ferric cytochrome P450cam and corresponding mutants using magnetic circular dichroism spectroscopy. *Biochemistry 50*, 1053−1069.

(65) Voegtle, H. L., Sono, M., Adak, S., Pond, A. E., Tomita, T., Perera, R., Goodin, D. B., Ikeda-Saito, M., Stuehr, D. J., and Dawson, J. H. (2003) Spectroscopic characterization of five- and six-coordinate ferrous-NO heme complexes. Evidence for heme Fe-proximal cysteinate bond cleavage in the ferrous-NO adducts of the Trp-409Tyr/Phe proximal environment mutants of neuronal nitric oxide synthase. *Biochemistry 42*, 2475−2484.

(66) Giroud, C., Moreau, M., Sagami, I., Shimizu, T., Frapart, Y., Mansuy, D., and Boucher, J. L. (2010) Comparison of wild type neuronal nitric oxide synthase and its Tyr588Phe mutant towards various L-arginine analogues. *J. Inorg. Biochem. 104*, 1043−1050.

(67) Li, D., Kabir, M., Stuehr, D. J., Rousseau, D. L., and Yeh, S. R. (2007) Substrate- and isoform-specific dioxygen complexes of nitric oxide synthase. *J. Am. Chem. Soc. 129*, 6943−6951.

(68) Ost, T. W., Munro, A. W., Mowat, C. G., Taylor, P. R., Pesseguiero, A., Fulco, A. J., Cho, A. K., Cheesman, M. A., Walkinshaw, M. D., and Chapman, S. K. (2001) Structural and spectroscopic analysis of the F393H mutant of flavocytochrome P450 BM3. *Biochemistry 40*, 13430−13438.

(69) Ost, T. W., Clark, J., Mowat, C. G., Miles, C. S., Walkinshaw, M. D., Reid, G. A., Chapman, S. K., and Daff, S. (2003) Oxygen activation and electron transfer in flavocytochrome P450 BM3. *J. Am. Chem. Soc. 125*, 15010−15020.

(70) Chen, Z., Ost, T. W., and Schelvis, J. P. (2004) Phe393 mutants of cytochrome P450 BM3 with modified heme redox potentials have altered heme vinyl and propionate conformations. *Biochemistry 43*, 1798−1808.

(71) Varadarajan, R., Zewert, T. E., Gray, H. B., and Boxer, S. G. (1989) Effects of buried ionizable amino acids on the reduction potential of recombinant myoglobin. *Science 243*, 69−72.

(72) Dutton, P. L., Shifman, J. M., Gibney, B. R., and Sharp, R. E. (2000) Heme redox potential control in de novo designed four-α-helix bundle proteins. *Biochemistry 39*, 14813−14821.

(73) Olea, C. Jr., Kuriyan, J., and Marletta, M. A. (2010) Modulating heme redox potential through protein-induced porphyrin distortion. *J. Am. Chem. Soc. 132*, 12794−12795.

(74) Gray, H. B., Tezcan, F. A., and Winkler, J. R. (1998) Effects of ligation and folding on reduction potentials of heme proteins. *J. Am. Chem. Soc. 120*, 13383−13388.

(75) Okamura, T., Takamizawa, S., Ueyama, N., and Nakamura, A. (1998) Novel rubredoxin model tetrathiolato iron(II) and cobalt(II) complexes containing intramolecular single and double NH···S hydrogen bonds. *Inorg. Chem. 37*, 18−28.

(76) Ueno, T., Nishikawa, N., Moriyama, S., Adachi, S., Lee, K., Okamura, T., Ueyama, N., and Nakamura, A. (1999) Role of the invariant peptide fragment forming NH···S hydrogen bonds in the active site of cytochrome P-450 and chloroperoxidase: Synthesis and properties of Cys-containing peptide Fe(III) and Ga(III) (octaethylporphinato) complexes as models. *Inorg. Chem. 38*, 1199−1210.

(77) Ueyama, N., Yamada, Y., Okamura, T., Kimura, S., and Nakamura, A. (1996) Structure and properties of $[\text{Fe}_4\text{S}_4\{2,6\text{-bis(acylamino)benzenethiolato-S}\}_4]^{2-}$ and $[\text{Fe}_2\text{S}_2\{2,6\text{-bis(acylamino)-benzenethiolato-S}\}_4]^{2-}$: Protection of the Fe-S bond by double NH···S hydrogen bonds. *Inorg. Chem. 35*, 6473−6484.